Supplementary Informantion for

A Broadband Lithium Tantalate-on-Silicon Nitride Heterogeneous Modulator for Optical and Terahertz Communications and Radar Sensing

Jinwei Su *et al.*

*Liangjun lu, luliangjun@sjtu.edu.cn

*Cheng Zeng, zengchengwuli@hust.edu.cn

*Junwen Zhang, junwenzhang@fudan.edu.cn

Supplementary Note 1: Design of the heterogenous modulator

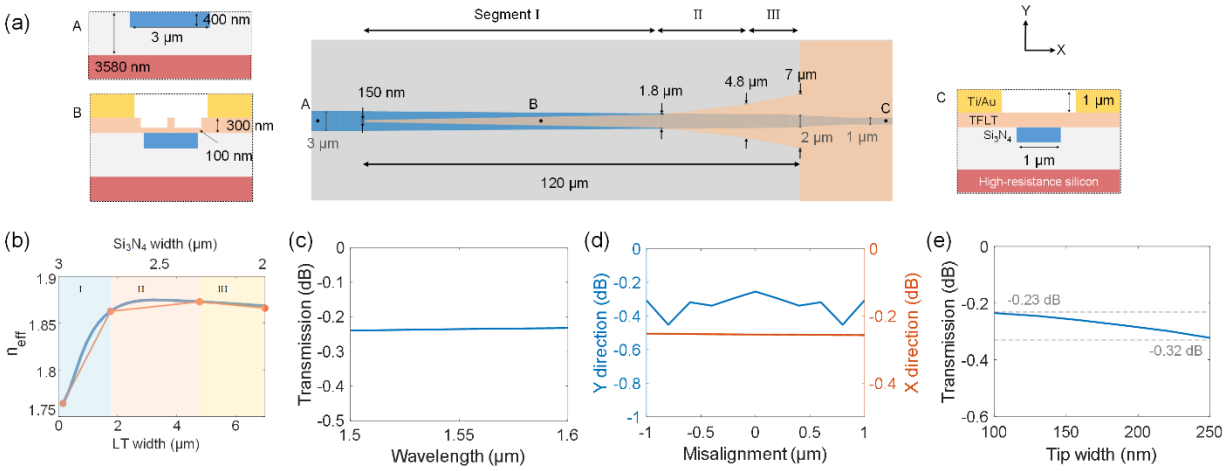

Fig. S1 Design of the interlayer coupler. (a) Schematic of the interlayer coupler. (b) n_{eff} of the hybrid waveguide vs waveguide width. (d) Transmission spectrum of the coupler. (e) Misalignment tolerance of the interlayer coupler in the direction of X and Y. (f) Fabrication tolerance of the TFLT tip.

The thickness of the Si_3N_4 waveguide is 400 nm, while the thickness of TFLT coupon is 300 nm. As shown in Fig. S1(a), an interlayer coupler is designed to reduce the coupling loss between the Si_3N_4 waveguide and the hybrid waveguide. To improve mode matching and alignment robustness, the Si_3N_4 strip beneath the coupler is widened to 3 μm (inset A of Fig. S1(a)) and then tapered to the final width. On top of this Si_3N_4 layer, a TFLT taper with a 100-nm-thick slab configuration transitions from a narrow tip to a quasi-infinite width, forming a hybrid TFLT-on-Si_3N_4 waveguide structure (insets B and C of Fig. S1(a)). First, the start and end widths of the TFLT taper are determined using the Lumerical FDE solver. The narrow tip width is set to 150 nm, which is compatible with fabrication capabilities. When the final width of the taper is insufficient to fully cover the underlying Si_3N_4 waveguide, additional loss can be introduced. For reliable performance, the Si_3N_4 and TFLT width are selected as 2 μm and 7 μm, respectively. Next, the taper length is determined by the Lumerical EME solver. Due to the large difference between the start and end widths, a length of 800 μm is required for a single taper to achieve adiabatic coupling under a 1 μm alignment tolerance. As long as the effective refractive index (n_{eff}) changes gradually, the optical mode in the taper evolves adiabatically[1]. Figure S1(b)

illustrates n_{eff} of the hybrid waveguide as a function of Si_3N_4 width and TFLT width. When the TFLT width is less than 1.8 μm, n_{eff} increases rapidly with width. Conversely, for widths exceeding 1.8 μm, n_{eff} varies more slowly. This indicates that a wider taper does not require an excessively long transition length. To optimize the design, the taper is divided into three linear segments (Segments I-III), each tailored to the local n_{eff} gradient with respect to hybrid waveguide width. The length of each taper segment is determined with the EME solver, resulting in a total TFLT taper length of about 120 μm. More design details can be found in our previous works[2, 3]. Finally, the designed coupler is verified by the Lumerical FDTD solver. The simulated transmission spectrum is shown in Fig. S1(c), demonstrating a low coupling loss of about 0.23 dB/facet over the 100 nm wavelength range. The misalignment tolerance is shown in Fig. S1(d). The coupler achieves an insertion loss of 0.23-0.45 dB within a ±1 μm misalignment tolerance in the Y direction, while remaining insensitive in the X direction. To evaluate fabrication tolerance, the TFLT tip width is varied from 100 nm to 250 nm, resulting in only a 0.1 dB increase in loss (Fig. S1(e)).

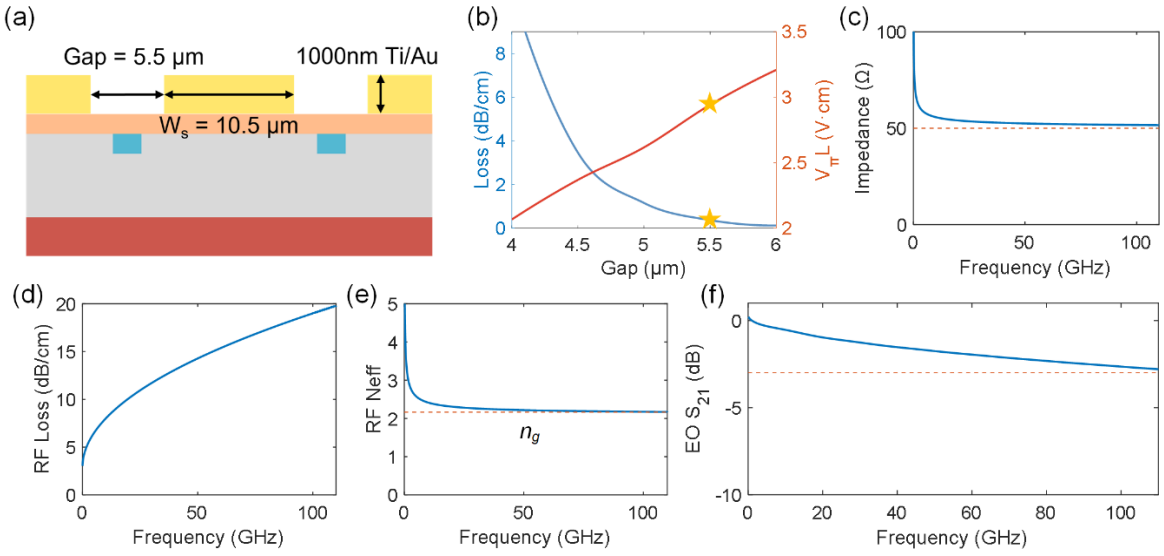

Fig. S2 Design of the traveling-wave electrodes of the MZM. (a) Cross-section of the MZM. (b) Simulated absorption loss and $V_\pi L$ versus electrode gap width. (c) The impedance of TWE versus RF frequency. (d) The attenuation of TWE versus RF frequency. (e) Phase matching between the optical and microwave waves. (f) Simulated EO response.

Then, the traveling-wave electrode (TWE) is designed. Figure S2(a) shows the cross-section of the MZM, while Fig. S2(b) highlights the optimized electrode gap of 5.5 μm.

This specific gap has been selected to strike a balance between absorption loss and modulation efficiency. As a result, the device achieves a propagation loss of 0.37 dB/cm and a push-pull VπL of 2.94 V·cm. The TWE thickness and signal electrode width are optimized through parameter sweeps and finalized at 1000 nm and 10.5 μm, respectively. To match the actual condition, the conductivity of metal gold is set to about 60% of the theoretical value. HFSS simulations confirm that the TWE provides an impedance of ~52 Ω, close to the standard 50 Ω, along with good velocity matching between the microwave effective index and the optical group index (n_g = 2.162), resulting in a 3-dB electro-optic bandwidth exceeding 110 GHz.

Supplementary Note 2: Statistical analysis of the transfer-printed MZIs

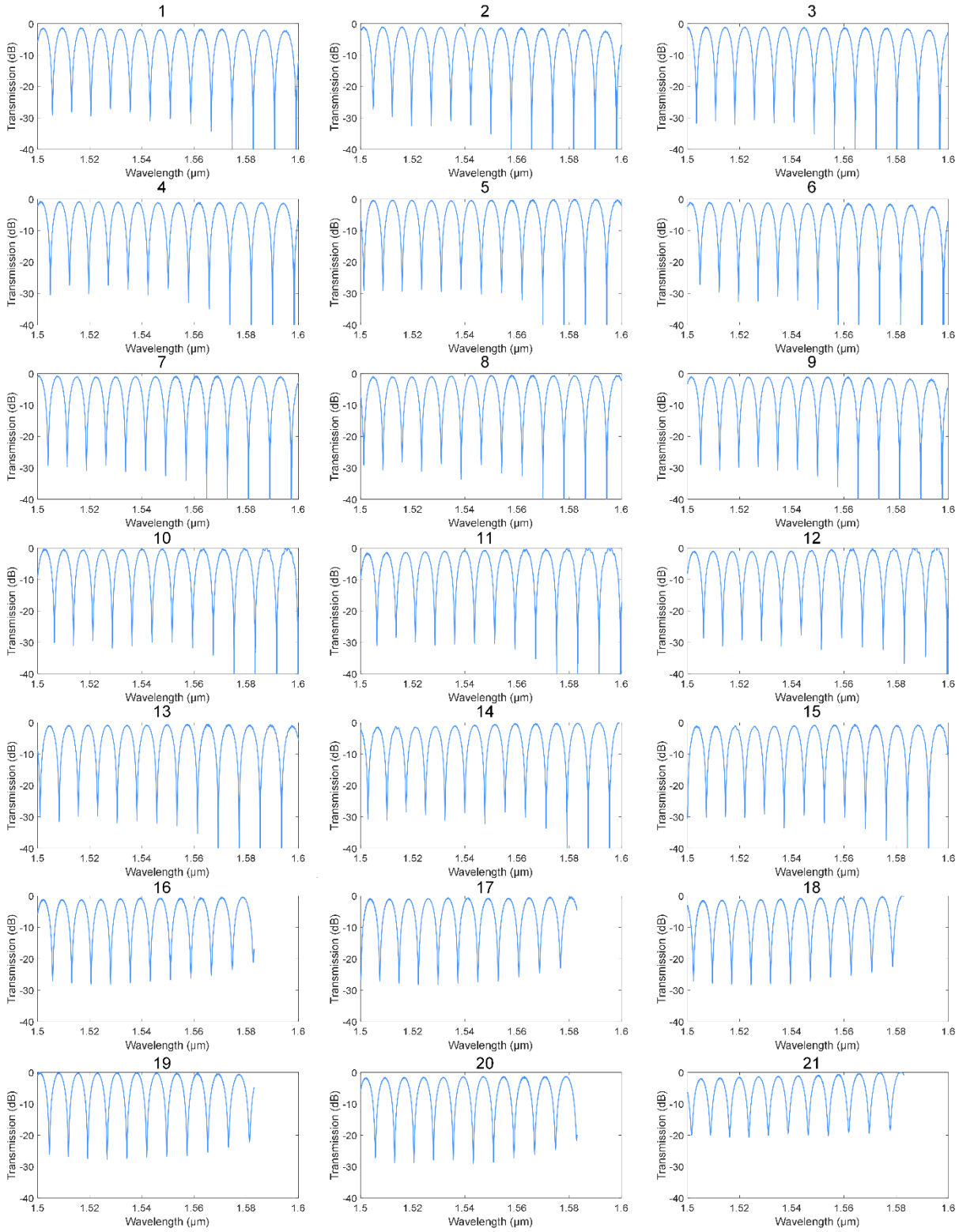

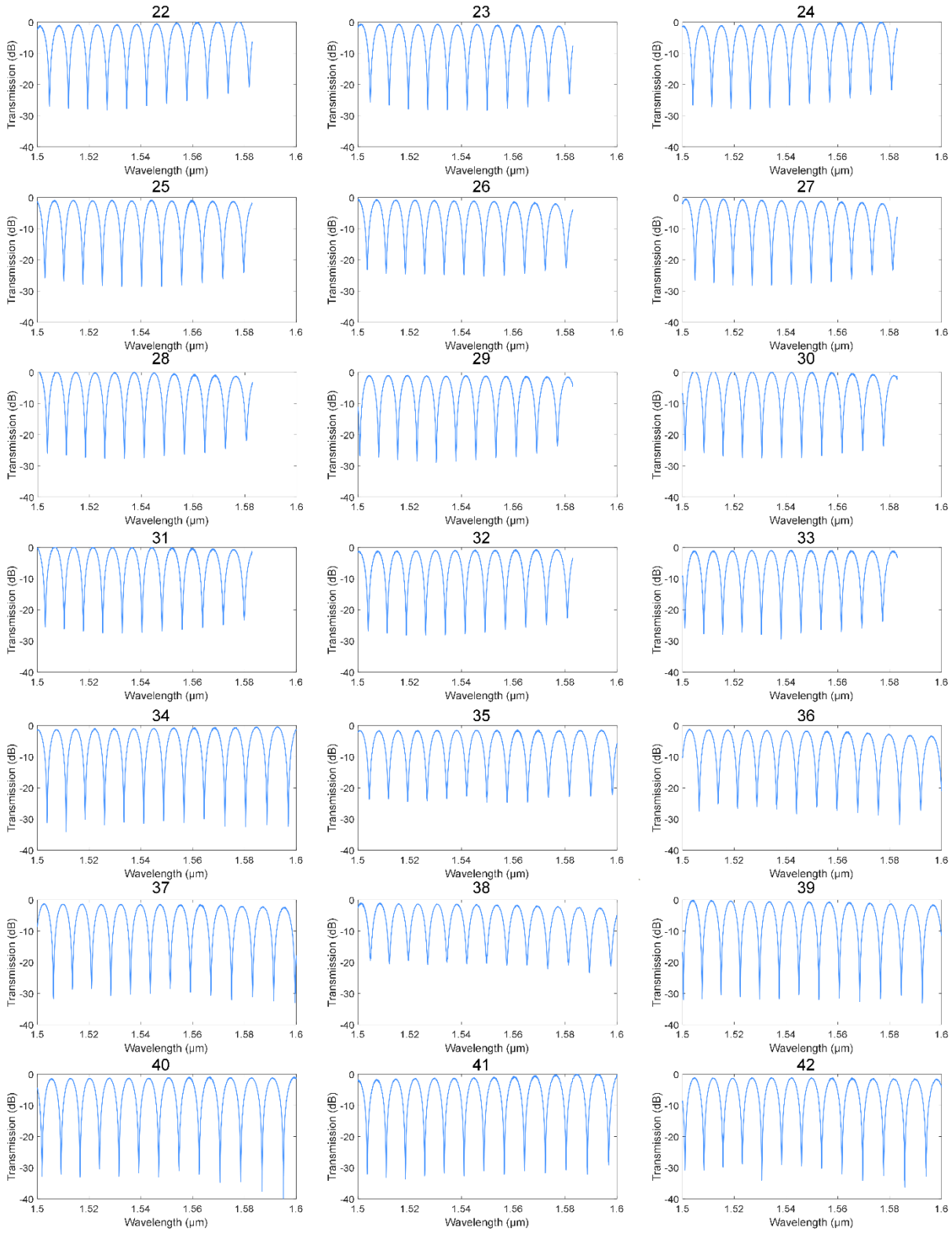

Fig. S3 Transmission spectra of 42 MZIs.

Supplementary Note 3: RF analysis of the MZM

Figure S4 depicts the measured S parameter of the MZM. As shown in Fig. S4 (a), the impedance of the MZM is close to 50 ohm with a slight fluctuation. As shown in Fig. S4 (b), the measured RF transmission loss is closed to the simulated results. As shown in Fig. S4 (c), the design attains an almost ideal velocity matching between the microwave and optical modes, especially at high frequency. Thus, the bandwidth limitation arises mainly from RF loss, mainly due to impurities in the deposited gold, which reduce its conductivity to about 60% of the theoretical value. This issue can be addressed by using higher-purity metals and fine-tuning the electron-beam evaporation conditions.

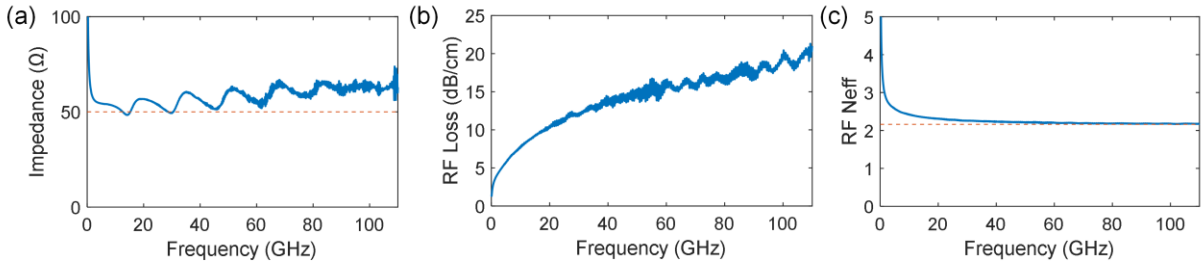

Fig. S4 Measured S parameter of the MZM. (a) Measured impedance versus RF frequency. (b) Measured attenuation versus RF frequency. (c) Measured RF effective index versus RF frequency.

Supplementary Note 4: Data transmission of the MZM

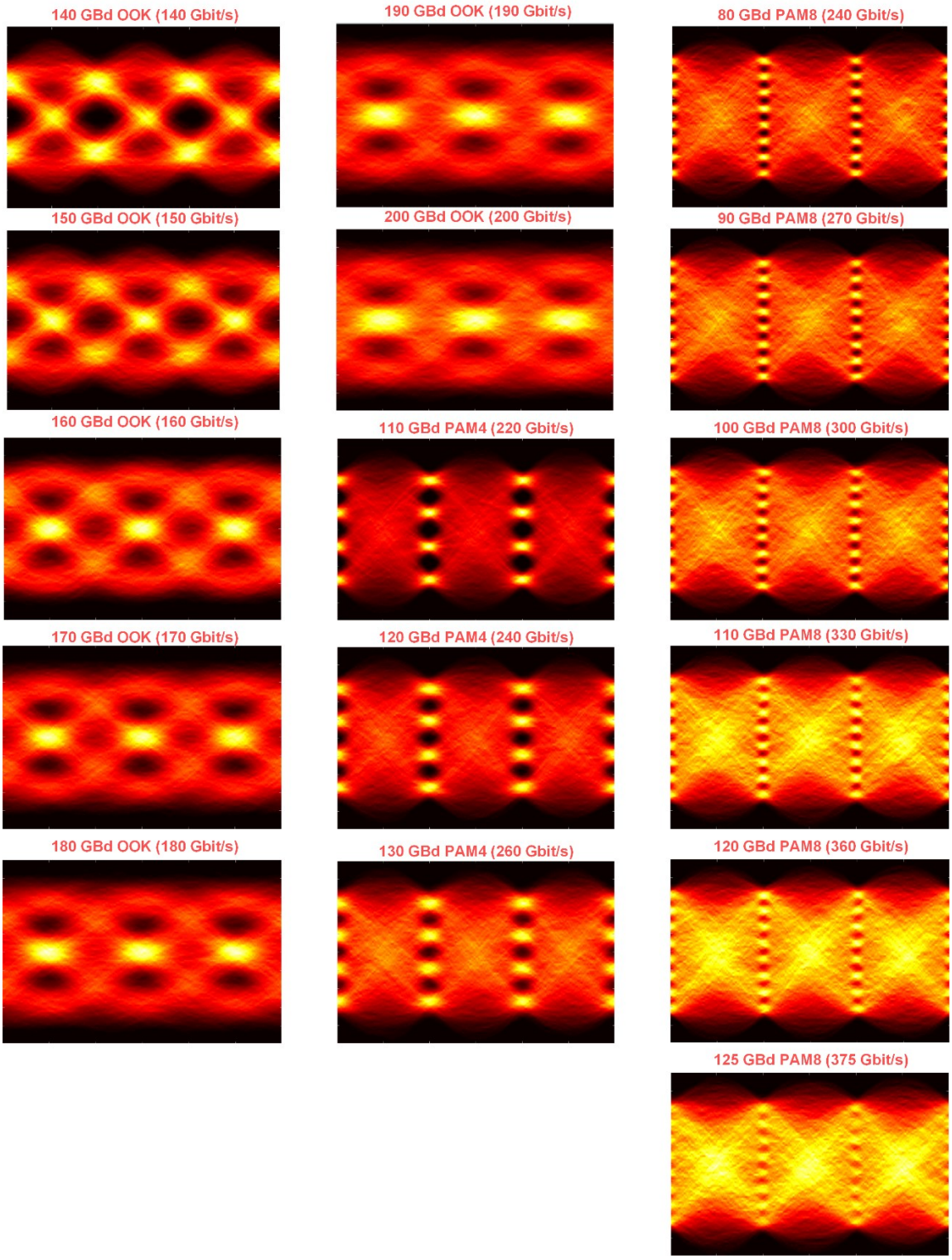

Fig. S5 Eye diagrams of single MZM with different symbol rate and different modulation format.

Supplementary Note 5: Wireless transmission of the MZM

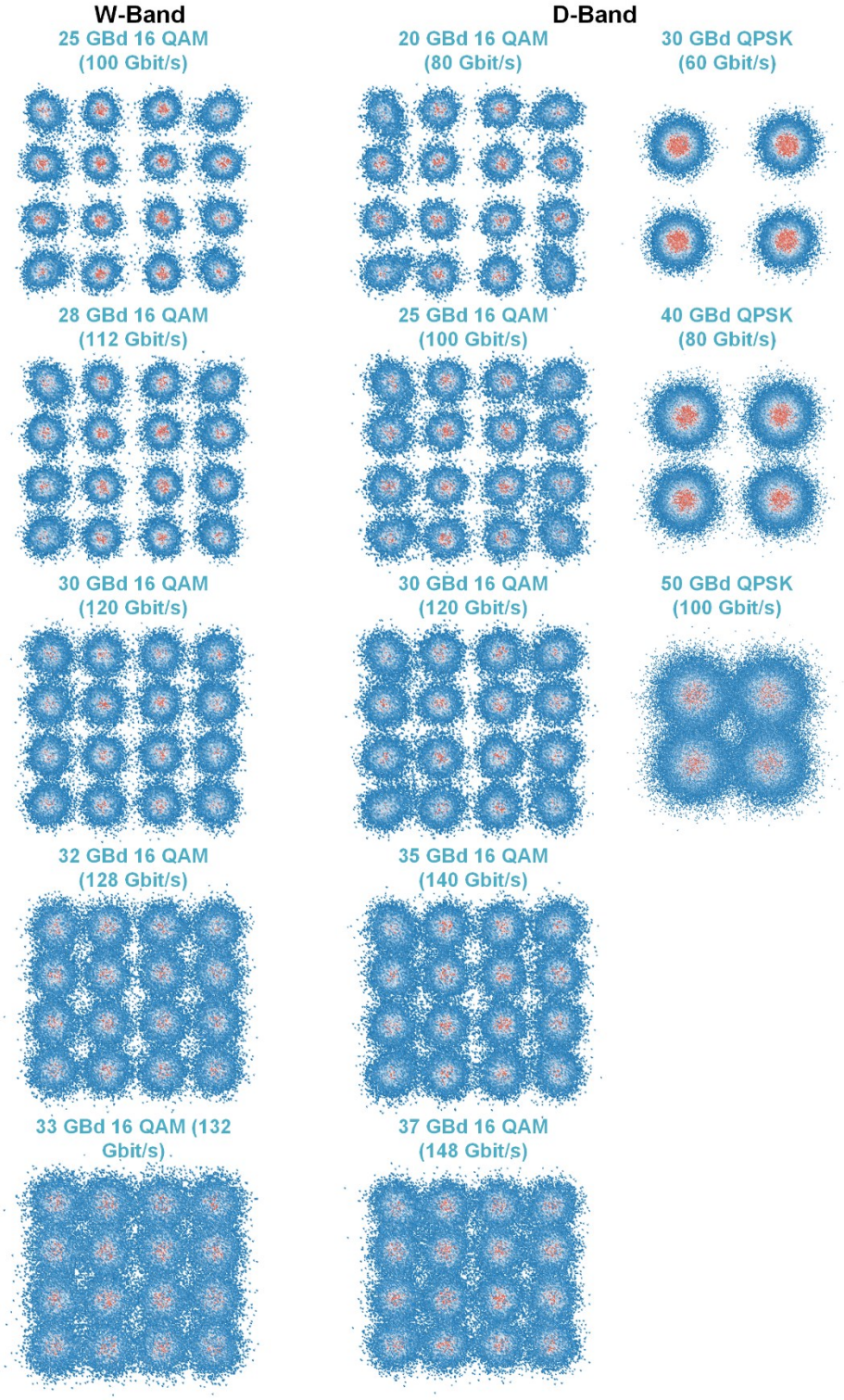

Fig. S6 Wireless data communication with different symbol rates and modulation formats in the W-band and D-band.

Supplementary Note 6: The principle of radar sensing

In this study, a linear frequency-modulated (LFM) signal was employed to realize radar sensing functionality. The LFM signal can be expressed as：

$$s_{LFM}(t) = rect\left(\frac{t}{T_{LFM}}\right) exp\{j2\pi f_0 t + j\pi k t^2\} \quad (1)$$

where T_{LFM} is the duration of the LFM pulse, f_0 is the initial frequency, and k denotes the chirp rate. The generated LFM signal was then applied to an in-phase/quadrature (IQ) optical modulator driven by the laser emitted from Laser 1. Under small-signal modulation, the output optical field of the IQ modulator can be expressed as

$$E_{IQM}(t) \propto E_{c1}\, exp(2j\pi f_{c1} t) \cdot exp[j\pi(2f_0 t + kt^2)] \quad (2)$$

where E_{c1} and f_{c1} represent the optical amplitude and frequency of Laser 1, respectively. The modulated optical signal was amplified by EDFA 1 and subsequently combined with the local oscillator (LO) light emitted from Laser 2. The combined optical field can be written as

$$E_{point-A}(t) \propto E_{IQM}(t) + E_{c2}\, exp(2j\pi f_{c2} t) \quad (3)$$

where E_{c2} and f_{c2} denote the amplitude and frequency of Laser 2. The combined optical signal was divided into two branches. One branch was directed into a PD to generate a W-band millimeter-wave signal via optical heterodyning, while the other branch served as the reference light for photonic de-chirping of the LFM echo signal. After optical-to-electrical (O/E) conversion, the generated millimeter-wave signal was amplified by a power amplifier (PA) and radiated into free space through a horn antenna (HA). Its transmission in the wireless channel can be represented as

$$E_{MMW}(t) \propto cos\left[2\pi\left(f_{c1} - f_{c2} + f_0 + \frac{kt}{2}\right)t\right] \quad (4)$$

For radar sensing, the transmitted signal is reflected by the targets in the scene, and the received echo can be expressed as：

$$E_{echo}(t) \propto cos\left\{2\pi\left[f_{c1} - f_{c2} + f_0 + \frac{kt}{2+k\tau}\right]t\right\} \quad (5)$$

where τ denotes the time delay. Subsequently, the echo signal is directly modulated onto the reference optical carrier containing the reference LFM waveform using the MZM. Owing to its broadband characteristic, the MZM enables direct reception and photonic de-

chirping of the LFM echo signal. Under small-signal modulation and when the MZM operates at the null point, the output optical field can be expressed as：

$$E_{point-B}(t) \propto \begin{Bmatrix} A_1 cos\left[2\pi\left(2f_{c2}-f_{c1}-f_0-\frac{kt}{2-k\tau}\right)t\right]+ \\ A_2 cos\left[2\pi\left(f_{c1}+f_0+\frac{kt}{2+k\tau}\right)t\right]+ \\ A_3 cos[2\pi(2f_{c1}-f_{c2}+2f_0+kt+k\tau)t]+ \\ A_4 cos[2\pi(f_{c2}-k\tau)t]+ \\ A_5 cos\left[2j\pi\left(f_{c1}+f_0+\frac{kt}{2}\right)t\right]+ \\ A_6 cos(2j\pi f_{c2}t) \end{Bmatrix} \tag{6}$$

where A_n denotes the amplitude of each component. The first term corresponds to the lower sideband generated by modulating the echo signal onto the LO light from Laser 2. The second term represents the upper sideband. The third term arises from broadband intermodulation between the echo and reference signals. The fourth term corresponds to the de-chirped LFM component whose frequency is approximately f_{c2}. And the fifth and sixth terms correspond to the input signal and LO light, respectively. These spectral components can be observed in the optical spectrum. After photonic de-chirping, the MZM output and the LO light from Laser 2 were fed into the coherent receiver (Co. Rx), enabling extraction of the time-delay information $k\tau$ contained in the fourth term.

In the experiment, the LFM signal was first generated in MATLAB and then split into in-phase (I) and quadrature (Q) components. The two components were individually fed into an AWG to perform digital-to-analog conversion. The generated LFM signal has a bandwidth of B_s and a duration of T_s, resulting in a chirp rate of $k = B_s/T_s$. The analog IQ signals from the AWG were subsequently applied to an IQ modulator (IQM) to modulate the optical carrier emitted by Laser 1, thus achieving IQ modulation. The modulated optical signal was amplified by EDFA1 and then combined with a local oscillator (LO) light generated by Laser 2 using an optical coupler (OC). The frequency difference between the signal light and the LO light determines the center frequency of the transmitted W-band millimeter-wave signal. The measured optical spectrum is shown in Fig. 6(b). The coupled optical signal is then split into two paths by a 50:50 OC. One branch was delivered to a PD, where a W-band millimeter-wave signal was generated through optical heterodyning. The other branch was used as a reference signal for photonic de-chirping of the received W-band LFM echo. After opto-electronic conversion,

the generated W-band signal was amplified by a PA and radiated into free space via a HA.

At the radar receiving end, the HA captured the W-band LFM echo signal reflected from the target in the scene. The received signal was first amplified by an LNA and then directly modulated onto the reference optical signal through the designed modulator, enabling photonic de-chirping. The optical spectrum at the modulator output, shown in Fig. 6(c), reveals distinct modulation depths corresponding to targets at different ranges. Because the de-chirped signal lies close to the optical frequency of the LO light emitted by Laser 2, the modulator output can be coherently combined with the LO light and fed into the Co.Rx, where photonic down-conversion and opto-electronic conversion are accomplished. After self-homodyne detection, the beat frequency associated with the target distance was obtained by fast Fourier transform (FFT). The relationship between the de-chirped beat frequency and the target distance can be expressed as (where Δf is the de-chirped frequency and c denotes the speed of light):

$$\Delta R = \frac{cT_s\Delta f}{2B_s} \tag{7}$$

Supplementary Note 7: Raw data of the DC drift measurement

The DC-drift measurement of the MZM without optical and electrical packages was performed on an optical coupling stage, as shown in Fig. S7(a). A continuous-wave laser was vertically coupled into the chip through a single-mode fiber, while a high-speed probe was used to apply the DC bias provided by an external voltage source (ITECH IT6133B). The optical source was a benchtop tunable laser (Agilent 8164B), and the received optical power was monitored using the built-in photodetector module of the same instrument (Agilent 81636B). After achieving optimal fiber alignment, the voltage source was switched on, and the optical power was automatically recorded at one-minute intervals using a computer-controlled data acquisition program. Since the chip was unpackaged, mechanical perturbations caused the fiber to deviate from the optimal coupling position over time, producing transient drops in measured power. During the intervals between data acquisitions, we manually realigned the fiber to the optimal position. Occasionally, when the external environment fluctuated significantly and the fiber alignment could not be adjusted in time, a severe drop in optical power occurred. The raw measurement data containing these events is shown in Fig. S7 (b). However, it can be observed that even after applying the DC bias for tens of hours (up to 72 h), the optical power remained close to its initial level once the fiber was realigned to the optimal coupling position. The results indicate that the intrinsic power drift of the device was relatively small. Thus, data points exhibiting anomalous power drops were identified as invalid due to fiber misalignment and were reasonably excluded from the analysis. At approximately 72 h, the power deviation after readjustment was only 0.38 dB; therefore, data with a power drift exceeding 1 dB were regarded as invalid and excluded, as presented in Fig. 3(f).

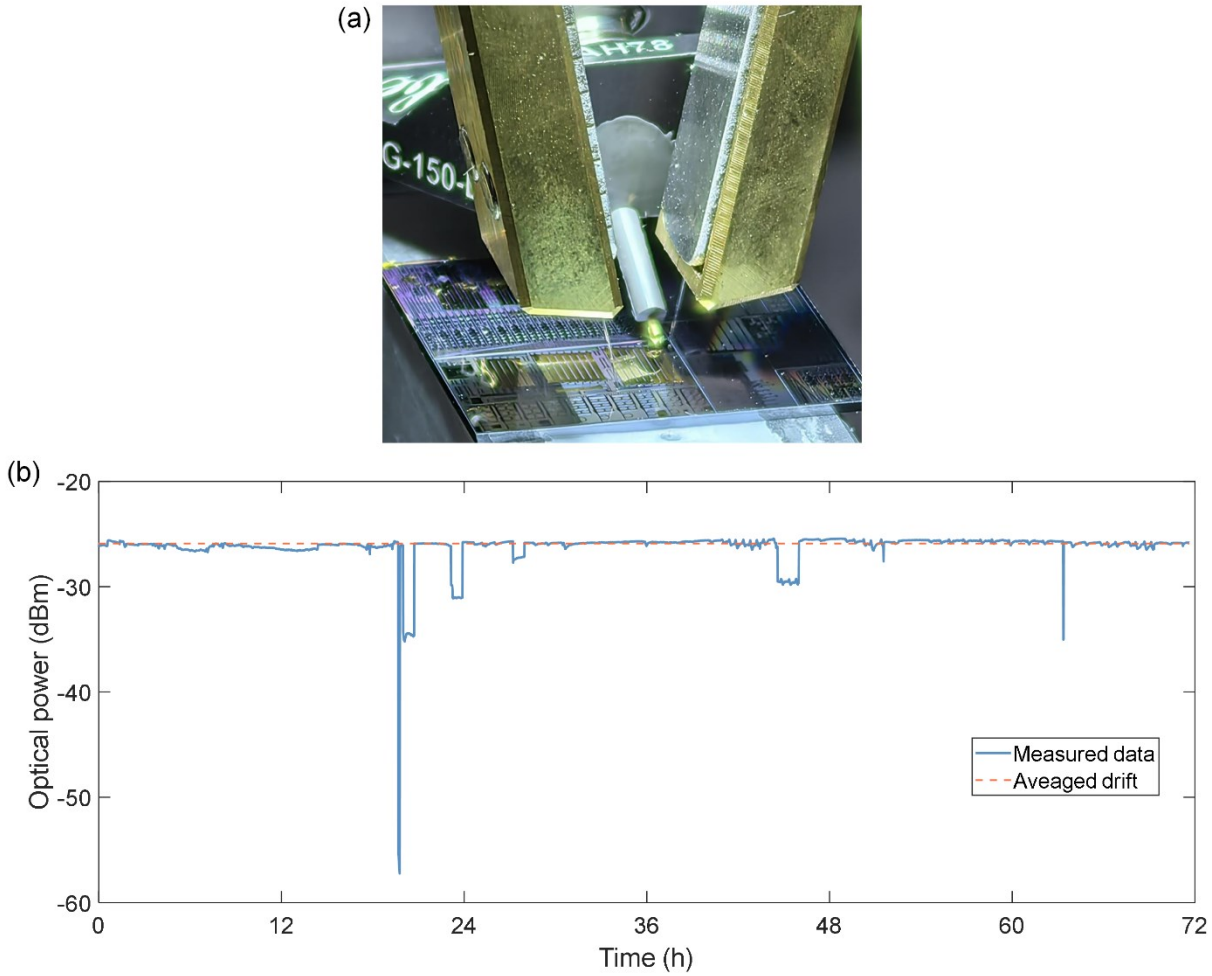

Fig. S7 DC drift measurement. (a) Measurement setup. (b) Raw data of the DC drift measurement.

References

1. Fu, Y., Ye, T., Tang, W. & Chu, T. Efficient adiabatic silicon-on-insulator waveguide taper. *Photon. Res.* **2**, A41 (2014).
2. Su, J. et al. Large-Area Microtransfer-Printed Thin-Film Lithium Niobate-Silicon Nitride Microring Optical Filter with Nanosecond Tuning Speed. *ACS Photonics* **12**, 2062-2069 (2025).
3. Su, J. et al. Ultralow-Loss Micro-Transfer Printed Thin-Film Lithium Niobate on Silicon Nitride Coupler. in 2024 *Asia Communications and Photonics Conference (ACP) and International Conference on Information Photonics and Optical Communications (IPOC)* 1-4 (IEEE, Beijing, China, 2024).